Check for updates

Excitons in a reconstructed moiré potential in twisted WSe$_2$/WSe$_2$ homobilayers

Trond I. Andersen[1,9], Giovanni Scuri[1,9], Andrey Sushko[1,9], Kristiaan De Greve[1,2,7,9], Jiho Sung[1,2], You Zhou[1,2], Dominik S. Wild[1], Ryan J. Gelly[1], Hoseok Heo[1], Damien Bérubé[3], Andrew Y. Joe[1], Luis A. Jauregui[1,8], Kenji Watanabe[4], Takashi Taniguchi[5], Philip Kim[1,6], Hongkun Park[1,2 ✉] and Mikhail D. Lukin[1 ✉]

Moiré superlattices in twisted van der Waals materials have recently emerged as a promising platform for engineering electronic and optical properties. A major obstacle to fully understanding these systems and harnessing their potential is the limited ability to correlate direct imaging of the moiré structure with optical and electronic properties. Here we develop a secondary electron microscope technique to directly image stacking domains in fully functional van der Waals heterostructure devices. After demonstrating the imaging of AB/BA and ABA/ABC domains in multilayer graphene, we employ this technique to investigate reconstructed moiré patterns in twisted WSe$_2$/WSe$_2$ bilayers and directly correlate the increasing moiré periodicity with the emergence of two distinct exciton species in photoluminescence measurements. These states can be tuned individually through electrostatic gating and feature different valley coherence properties. We attribute our observations to the formation of an array of two intralayer exciton species that reside in alternating locations in the superlattice, and open up new avenues to realize tunable exciton arrays in twisted van der Waals heterostructures, with applications in quantum optoelectronics and explorations of novel many-body systems.

Engineered moiré superlattices that arise from lattice mismatch or relative twist angle between layers can induce periodic potentials for charge carriers and excitons. Although conceptually related to quantum simulation experiments, such as those in optical lattices[1], these systems feature the advantages of on-chip integrability, electronic tunability and small (nanometre) length scales. Moiré superlattices in semiconductor van der Waals (vdW) materials, such as transition metal dichalcogenides (TMDs), are attractive for this purpose due to the presence of optically active, tightly bound excitons[2]. Theoretical studies predict that these systems can be used to create topologically non-trivial states[3,4], atomically thin mirrors for quantum optical applications[5] and Hubbard model simulators[6] analogous to those based on trapped atom arrays[7]. Recent experiments explored the effects of moiré patterns in heterobilayers of TMDs, which included MoSe$_2$/WSe$_2$ (refs [8–11]), MoSe$_2$/WS$_2$ (ref. [12]), MoSe$_2$/MoS$_2$ (ref. [13]) and WS$_2$/WSe$_2$ (ref. [14]). Photoluminescence and absorption measurements in those experiments suggest that the periodic moiré potential can cause the trapping of interlayer exciton states[8,9], hybridization between bands in opposite layers[12] and multiple intralayer exciton states[14]. Most recently, a growing interest has developed in twisted TMD homobilayers[4,15–18], in which the moiré lattice is governed only by the relative twist angle and not by lattice constant mismatch, which enables experimental access to a larger range of superlattice length scales. This system was shown to exhibit superconductivity[15], and theoretically predicted to display a topological insulator behaviour as well as two-orbital Hubbard physics[4,16].

A major challenge within this field involves correlating the optical response with the imaging of the moiré lattice, which is necessary to draw unambiguous conclusions, disentangle extraneous effects and investigate the role of moiré length scales. Although direct imaging of the small (≲100 nm) moiré domains can be achieved through transmission electron microscopy[14] or scanning probe microscopy[19], such imaging techniques require special sample preparation, which has previously prevented optoelectronic measurements of the same device. Therefore, recently there have been substantial efforts to develop new imaging techniques, which include piezoresponse force microscopy[20], conductive atomic force microscopy[21] and scanning nearfield optical microscopy[22].

An alternative route to these scanning probe methods involves different forms of electron microscopy. Although scanning electron microscopy (SEM) techniques are used extensively for crystallographic imaging, the typical mode of operation relies on the detection of backscattered primary electrons[23,24], which is not efficient enough to probe mono- or bilayer materials. Nevertheless, in recent studies of conventional, covalently bonded semiconductors, it was pointed out that a subtle interplay between the channelling of primary electrons through a lattice and the extreme depth dependence of the generation of secondary electrons[25] allows for a direct imaging of the surface lattice ordering of SiC.

Here we demonstrate SEM-based imaging of the local atomic stacking order in a range of two-dimensional (2D) materials. This technique, which we refer to as 'channelling modulated secondary electron imaging', is compatible with typical devices used widely in

[1]Department of Physics, Harvard University, Cambridge, MA, USA. [2]Department of Chemistry and Chemical Biology, Harvard University, Cambridge, MA, USA. [3]Department of Physics, California Institute of Technology, Pasadena, CA, USA. [4]Research Center for Functional Materials, National Institute for Materials Science, Tsukuba, Japan. [5]International Center for Materials Nanoarchitectonics, National Institute for Materials Science, Tsukuba, Japan. [6]John A. Paulson School of Engineering and Applied Sciences, Harvard University, Cambridge, MA, USA. [7]Present address: imec, Leuven, Belgium. [8]Present address: Department of Physics and Astronomy, UC Irvine, Irvine, CA, USA. [9]These authors contributed equally: Trond I. Andersen, Giovanni Scuri, Andrey Sushko, Kristiaan De Greve. ✉e-mail: hongkun_park@harvard.edu; lukin@physics.harvard.edu
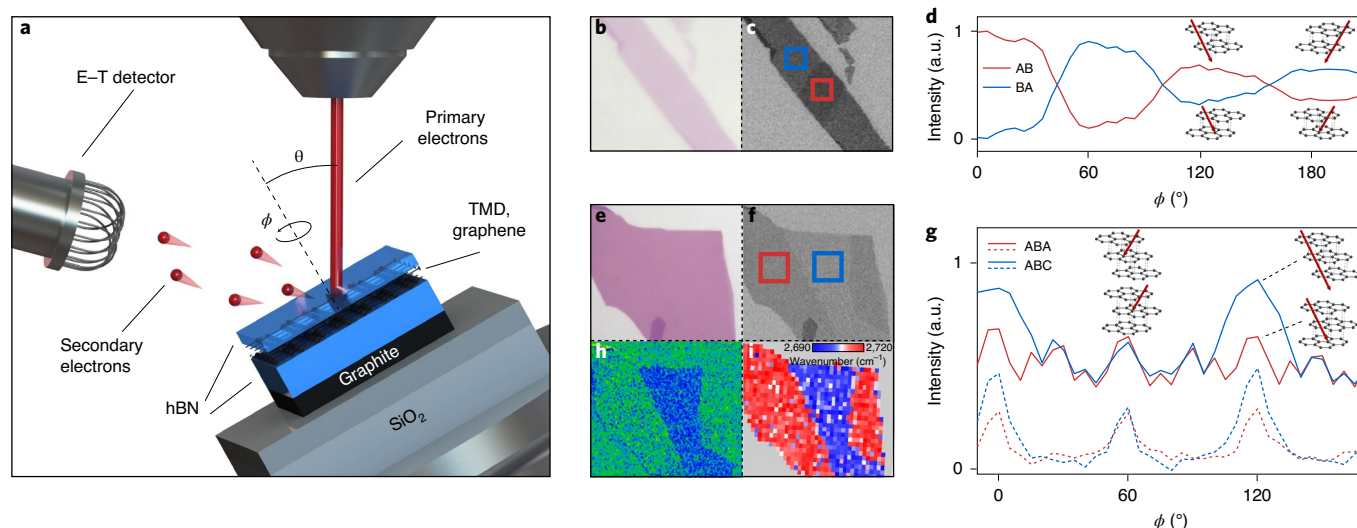
Fig. 1 | SEM-based imaging of stacking order in vdW heterostructures. a, Schematic of operating principle: an accelerated electron beam is focused onto the device at ϕ and θ. Channelling of the incident electrons and subsequent secondary electron generation depend on the local stacking order. **b,c**, Optical (**b**) and SEM (**c**) images of a natural bilayer graphene flake ($\theta = 24°$, $\phi = 5°$). SEM reveals areas of different contrast. **d**, Dependence of the SEM signal on ϕ in the boxed locations in **c** (normalized to the mean). The two regions display a 120° symmetry and 60° phase offset, consistent with AB and BA domains. The contrast decays due to gradual charging of the substrate. Inset: schematics of the atomic lattices. **e–g**, The same as in **b–d**, but for a few-layer (about six) graphene flake. The more complex ϕ dependence is consistent with our model of ABC and ABA stacking (dashed line; see Supplementary Note II for further details about the model): the ABC stacking exhibits fully open channels every 120°, whereas ABA stacking shows only partially open channels every 60°. **h**, Difference between two SEM images with a 60° offset in ϕ. **i**, Spatial map of Raman 2D-peak position, which confirms the ABC/ABA stacking order. a.u., arbitrary units. E–T, Everhart–Thornley.

the field, which include complete hexagonal BN (hBN) encapsulation, electrostatic gates, generic (for example, Si/SiO$_2$) substrates and no special sample fabrication. Crucially, it enables us to correlate imaged moiré patterns with optoelectronic measurements in twisted WSe$_2$/WSe$_2$ bilayers.

Channelling modulated secondary electron imaging technique

Our approach, illustrated in Fig. 1a, is based on measuring secondary electron emission, which depends on the scattering cross-section experienced by the incident primary electron beam as well as the escape depth of the secondary electrons. By placing the device at an angle, different stacking orders exhibit different channelling conditions, which thus gives rise to a signal contrast between them.

To illustrate how the technique resolves the atomic stacking order in vdW heterostructures, we first considered naturally occurring stacking domains in graphene. Besides representing a simple model system due to its monoatomic and purely 2D structure, stacking domains in graphene have been shown to exhibit exciting novel physical phenomena, which include the observation of Mott insulator and superconducting states in ABC-stacked trilayer graphene[26], and topologically protected states along the AB/BA boundaries in bilayer graphene[22,27,28].

Figure 1b,c shows images of a bilayer graphene flake on a Si/SiO$_2$ substrate, acquired by optical microscopy and SEM, respectively. Although the former is homogeneous, which confirms that the flake had a uniform thickness, SEM imaging at a 24° tilt angle and a small acceleration voltage of 500 eV uncovered two types of distinct domains. As the stage was rotated azimuthally, the intensity of the collected secondary electrons exhibited 120° periodic oscillations, with a 60° phase shift between the two domain types (Fig. 1d). The contrast was found to gradually decrease when the polar angle (θ) was moved away from 24° and to reappear near 40° (Supplementary Note I). We attribute the observed domains to different levels of electron channelling through naturally occurring regions of AB-

and BA-stacked graphene[27–29]. Such channelling arose at particular polar and azimuthal angles (ϕ), when the incoming electron beam was oriented parallel to the open cavities or 'channels' within the atomic lattice (Fig. 1d, inset), which allowed the electrons to travel through the material with minimal scattering. Consistent with our observations, the open cavities are expected to appear when $\theta = \tan^{-1}\left(\frac{n a_{gr}}{d_{gr}}\right) = 24°$, where n is an integer ($n = 1$ here), a_{gr} is the graphene atom–atom spacing and d_{gr} is the interlayer spacing. Moreover, optimal channelling conditions appear when ϕ is aligned with one of the three in-plane displacement vectors between the top and bottom layers, which thus causes the observed 120° periodicity and the 60° relative angle between the AB and BA domains. As graphene has a lower atomic number, Z, than that of the substrate (SiO$_2$), it generates fewer secondary electrons[30]. Thus, for graphene on oxide substrates, the secondary yield maxima occur when channelling is maximized.

Turning to a thicker (approximately six-layer) graphene flake, which also exhibited domains in SEM imaging that were not observable optically (Fig. 1e,f), we found a more complex azimuthal dependence (Fig. 1g). While one domain type (red) was 60° periodic in ϕ, the other (blue) exhibited a period of 120°, which reflects a lower inherent symmetry (Fig. 1h). Based on a simple channelling model (dashed lines in Fig. 1g and see Supplementary Notes II and III), we attribute this more complex pattern to ABA- and ABC-stacking orders[31], as independently verified with Raman spectroscopy[32] through the position of the Raman 2D peak (Fig. 1i; see Supplementary Note IV for representative spectra). Indeed, consistent with our observations, the two domain types are expected to have similar scattering cross-sections at certain ϕ values (Fig. 1g, left inset), but at other angles, the ABC domain allows for 'complete channelling' (Fig. 1g, right inset), giving rise to enhanced SEM signal every 120°.

Having demonstrated the ability to differentiate different stacking orders in few-layer graphene, we turned to a twisted WSe$_2$/WSe$_2$ bilayer device (D1 (Fig. 2)), motivated by the fact that moiré
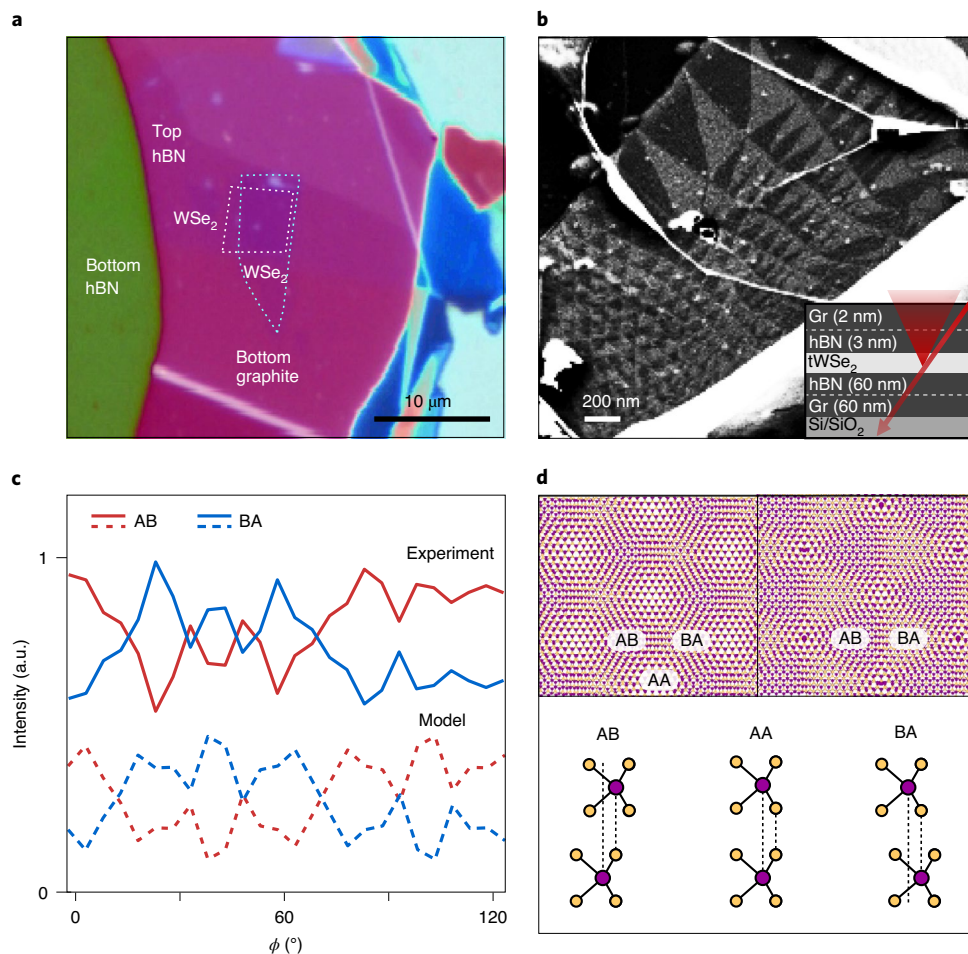
Fig. 2 | Moiré superlattices in twisted homobilayers. a, Optical image of hBN-encapsulated twisted WSe$_2$ bilayer (device D1). The dashed white and teal lines indicate the top and bottom TMD layers, respectively. **b**, SEM image of device D1 showing a reconstructed moiré pattern with triangular AB and BA (3R) stacking domains ($\theta = 40°$). Inset: device schematic (tWSe$_2$, twisted bilayer WSe2). **c**, ϕ dependence of signals from the AB and BA domains, along with model predictions (dashed curves). **d**, Top: top view schematic of the moiré pattern (5° twist angle) with and without reconstruction (right and left, respectively). The reconstruction was created by reducing the local twist angle near the AB and BA sites. Bottom: side view of AB, AA and BA stacking orders. Purple, W; yellow, Se.

patterns are periodic variations between AB and BA stacking orders[8,14]. We fabricated a fully functional device (Fig. 2a), which included few-layer graphene gates for electrostatic tuning and encapsulation in hBN, which is widely used to improve the optical and electronic properties of 2D materials. To image the TMD layers embedded in the heterostructure, we found that the acceleration voltage had to be increased to 3 keV so that secondaries could escape from within the heterostructure (Supplementary Notes V and VI). Moreover, as the lattice constant and interlayer spacing is different in WSe$_2$ from that in graphene, a different θ must be used. To simultaneously maximize the interaction volume, we used a shallow angle,

$$\theta = \tan^{-1}\left(\frac{3a_{WSe_2}}{d_{WSe_2}}\right) \approx 40°,$$ which corresponds to three lattice shifts.

Following these considerations, the SEM technique enabled imaging of a moiré pattern in the small (<1°) twist angle WSe$_2$/WSe$_2$ bilayer (Fig. 2b). Owing to the 3D structure of TMDs, we observed a more complex ϕ dependence than that in graphene (Fig. 2c), which is, nevertheless, captured well by our model, which takes the full lattice structure into account (dashed lines in Fig. 2c, and see Supplementary Note II). Moreover, the bright regions correspond to less channelling because, in contrast to graphene, the constituent elements of WSe$_2$ have a higher Z than that of the SiO$_2$ substrate and therefore a higher secondary electron yield.

Crucially, the imaged moiré pattern exhibited atomic reconstruction, in which the lattices were strained locally to maximize the size of the energetically favourable AB and BA (3R) stacking domains (Fig. 2d, top right)[19–21,33,34]. This reconstruction mechanism resulted in a triangular array of alternating AB/BA regions, as opposed to gradual transitions between the two domain types in a canonical moiré picture (Fig. 2d, top left)[33]—the latter is more prevalent at larger twist angles and in heterobilayers with an intrinsic lattice mismatch[7,14].

The SEM imaging directly demonstrates that the local moiré periodicity varies considerably across and within each of our devices, which highlights the necessity of imaging. This inhomogeneity was also observed in a similar hBN-encapsulated and gated device (D2, Fig. 3a), with a target twist angle of 2.5°, close to the theoretically proposed critical angle for reconstruction[21,34]. In particular, SEM imaging showed that the reconstructed moiré wavelength was $\lambda_m \approx 60$ nm on the right side of the device, and gradually decreased towards the left until the reconstructed moiré pattern was no longer observed ($\lambda_m < 10$ nm, left side of the dashed line in Fig. 3a). As a domain size of 10 nm is near the threshold for reconstruction, it is likely that the moiré pattern was not fully reconstructed in this left region, which may also play a part in its reduced visibility.
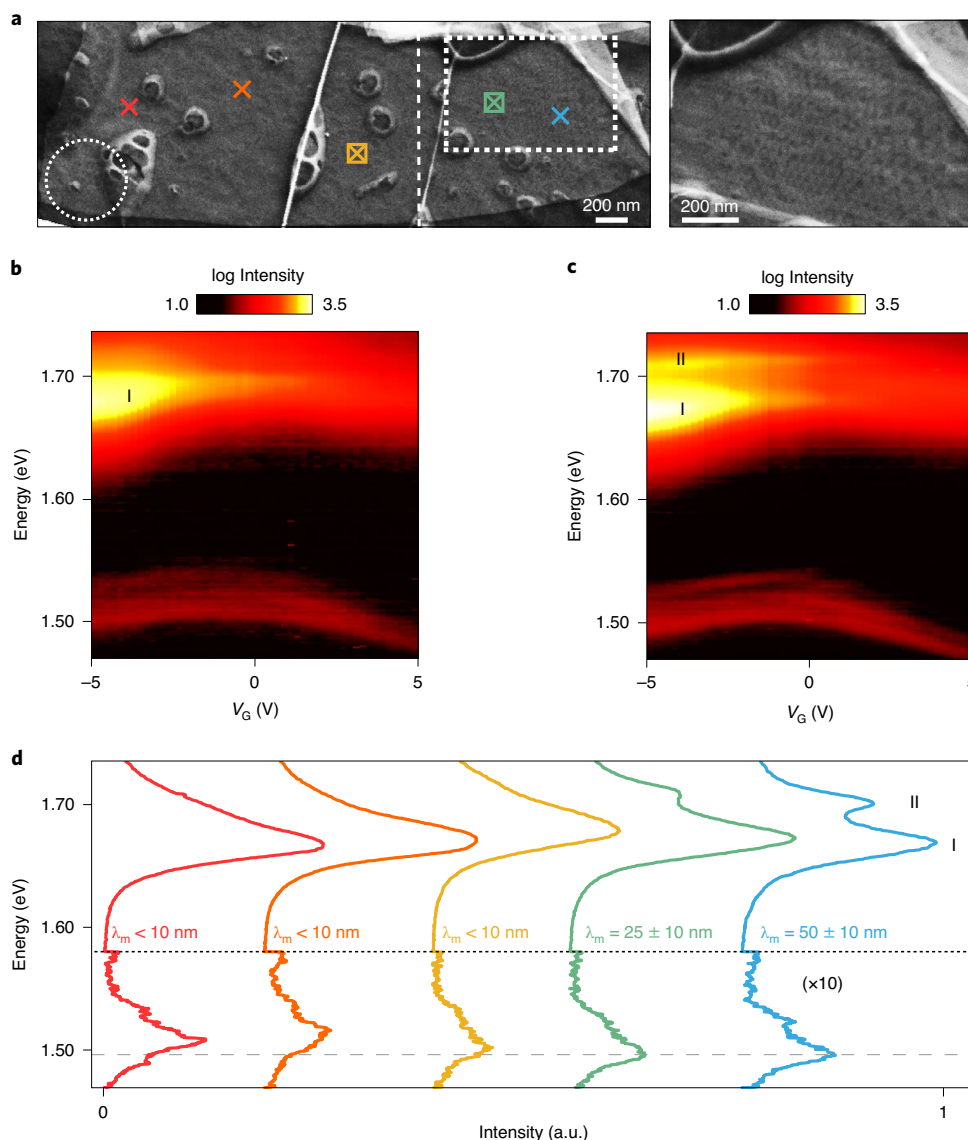
Fig. 3 | Correlating the local superlattice structure and optical properties. a, Left: SEM image ($\theta = 40°$) of device D2 displaying a reconstructed moiré pattern. λ_m increases from <10 nm to 60 nm from left to right. The moiré pattern is not visible left of the vertical dashed line. The dashed circle indicates the optical beam spot size and the crosses indicate the beam spot centres. Right: close-up of the area indicated by dotted lines. **b,c**, Gate-dependent PL spectra collected from locations with $\lambda_m < 10$ nm (**b**) and $\lambda_m = 25 \pm 10$ nm (**c**), indicated by the boxed crosses in **a**. While the left region only exhibits one intralayer peak in the p-doped regime, the right (larger λ_m region) exhibits two peaks. **d**, Raw PL spectra collected from the locations marked with crosses in **a**, at $V_G = -5$ V. The spectra are offset for clarity and the intensity is multiplied by 10 below 1.58 eV. The higher-energy (type II) exciton peak emerges with increasing λ_m, and the interlayer exciton emission is blueshifted for $\lambda_m < 10$ nm.

Correlating reconstructed moiré patterns with optical measurements

As the SEM-based imaging technique is compatible with fully functional devices, we could explore correlations between the moiré wavelength observed in SEM and the local optoelectronic properties. In particular, device D2 also enabled us to explore excitonic properties in the structural transition from the reconstructed to non-reconstructed regime. After co-aligning the SEM image with a map of photoluminescence (PL) intensity (see Supplementary Note VII for details), we collected gate-dependent PL spectra from both sides of the device (boxed crosses in Fig. 3a) in locations at which $\lambda_m < 10$ nm and $\lambda_m = 25 \pm 10$ nm (Fig. 3b,c, respectively). Owing to the diffraction-limited spot size and the aforementioned inhomogeneity, we note that each optical measurement probed a finite range of domain sizes, as indicated by the uncertainty range in λ_m.

In both spots, we observed two sets of emission features: the peaks near 1.5 eV are attributed to momentum-indirect interlayer excitons based on their energy[17,35], whereas the higher-energy peaks near 1.7 eV are attributed to K-valley momentum-direct intralayer excitons, consistent with previous studies[35–37] and absorption measurements (Supplementary Note VIII). Although only one intralayer exciton peak (peak I) was observed on the left side of the device (Fig. 3b, $\lambda_m < 10$ nm), an additional higher-energy peak (peak II) emerged in the right part (Fig. 3c, $\lambda_m = 25 \pm 10$ nm). Their splitting was 36 meV in the p-doped regime, where the two peaks were most pronounced, and decreased to 16 meV in the intrinsic regime (Supplementary Note IX). Besides their resonance energies, the doping dependence of peaks I and II was also distinct: with increasing hole doping, peak I broadened and intensified strongly, whereas peak II was much less affected.
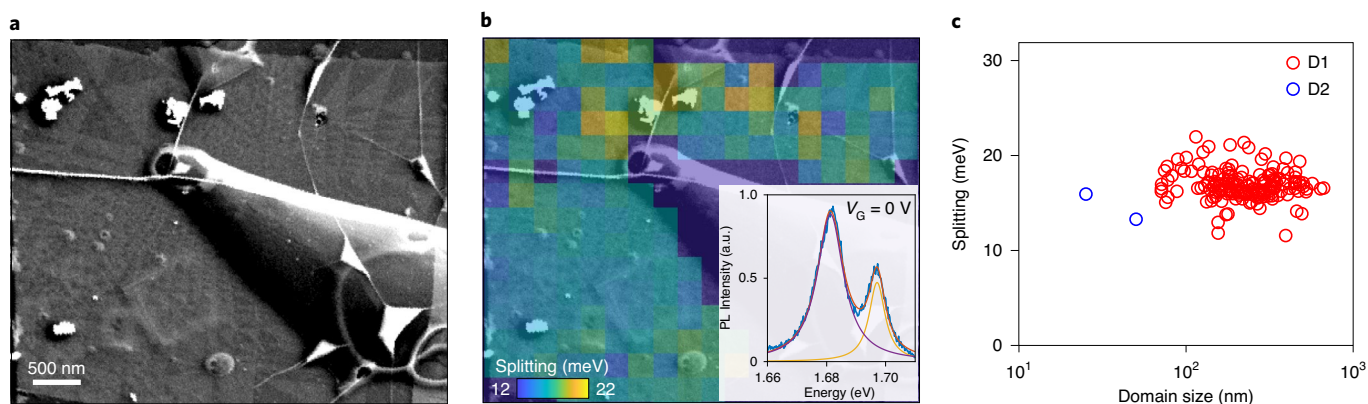
Fig. 4 | SEM correlation of PL peak splitting. a, Zoomed-out SEM image of D1 showing large (70–670 nm) reconstructed moiré domains in the entire twisted bilayer region ($\theta = 40°$). **b,** Map of extracted exciton-peak splitting overlaid with the SEM image from **a**. Inset: example PL spectrum (blue) with a double Lorentzian fit. **c,** The correlation of SEM and PL shows that the peak splitting is independent of domain size over a 30-fold range.

Inspecting more locations (crosses in Fig. 3a) at gate voltage $V_G = -5$ V, we found that a single dominant intralayer peak appeared in all the spots investigated on the left side of the device ($\lambda_m < 10$ nm), and that the higher-energy peak only emerged with the larger λ_m in the right region (Fig. 3d), in which the reconstructed moiré domains are observed. Consistent with these observations, the two intralayer exciton peaks were also observed in all of our devices with small twist angles (0–0.5°; Supplementary Note X), and the higher-energy peak was absent in all large-angle devices (5–22°; Supplementary Note X). We also found that the interlayer exciton peak was blueshifted in the left (small λ_m) region. This is not expected to be due to interlayer contamination (further details in Supplementary Note XI), but rather to the weaker interlayer coupling in the small-domain regime[17,35,38,39], which is also expected to cause less lattice reconstruction[21,34].

Previous studies of non-reconstructed moiré patterns in twisted heterobilayers[9,14,40,41], as well as recent theoretical predictions for twisted homobilayer WSe_2 (ref. [42]), considered exciton multiplets that arise from the moiré-induced mixing of exciton Bloch states $k = 0$ and $k = k_m$ (where k_m is a moiré wavevector), due to band folding and miniband formation. In that case, the splitting between the states, $E(k_m) - E(0) \approx \lambda_m^{-2}$, is strongly dependent on domain size[14,40–42]. To investigate whether this is the case for the two exciton states observed here, we turned to the smaller-angle device D1, which had both larger moiré domains and a greater variation in their size (Fig. 4a). Importantly, this device exhibited the same two-peak structure as that of device D2 (Fig. 4b, inset), with a very similar splitting in both the p-doped (36 meV) and intrinsic (16 meV) regimes (Supplementary Note IX). By spatially correlating the PL signal with SEM imaging (Fig. 4b), we found that the splitting is independent of domain size over a 30-fold range (25–670 nm, Fig. 4c), in stark contrast to previous observations in TMD heterostructures[9,14].

Device D1 also exhibited more-pronounced features in the n-doped regime, which showed a very different behaviour to that in the p-doped regime. Although peak I redshifted much more than peak II at the onset of the p-doped regime ($E_h^I = 20$ meV, $E_h^{II} \approx 0$ meV), peak II exhibited a larger redshift in the n-doped regime ($E_e^{II} = 16$ meV and $E_e^I = 11$ meV; dashed green arrows in Fig. 5a), and thus reduced the splitting to only 10 meV (see Supplementary Note VIII for an equivalent behaviour in absorption measurements and Supplementary Note IX for the fitting procedure).

To further explore the origin of the two exciton peaks, we conducted polarization-resolved photoluminescence spectroscopy. By illuminating with linearly polarized light, we excited a superposition of K and K′ valley excitons (excited by the superposition of σ^+ and σ^- photons), and subsequently measured the quantum coherence between these valley states by comparing the parallel and perpendicular emission components[43]. Importantly, we note that this measurement is very distinct from circularly polarized PL measurements[44], which probe the valley depolarization rate, not the quantum coherence[43,45] (Supplementary Note XII). Defining the degree of linear polarization, $DOLP = (I_\parallel - I_\perp)/(I_\parallel + I_\perp)$, where $I_\parallel (I_\perp)$ is the intensity of emission with parallel (perpendicular) polarization, we found that the two exciton species had very distinct coherence properties. The lower-energy (type I) exciton had almost no DOLP in the p-doped regime, whereas the higher-energy (type II) exciton exhibited a DOLP of up to 18% (Fig. 5b,c). When entering the neutral regime, the DOLP of the type I exciton increased strongly and exceeded that of type II, which exhibited much less change. In the n-doped regime, the DOLP of both exciton types was found to be even higher, up to 44% (Fig. 5b,d). We note that very similar doping-dependent behaviour and valley coherence properties were also observed in several other small twist-angle WSe_2/WSe_2 devices (Supplementary Notes XIII and XIV).

Properties of the reconstructed superlattice

We here show that all our observations are consistent with two spatially alternating, individually controllable exciton species in the reconstructed superlattice. Our model is based on the local band structure differences in the observed AB- and BA-stacked domains of twisted WSe_2/WSe_2. As AB and BA domains are vertical mirror images of each other, we refer to the top layer in the BA domains and the equivalent bottom layer in the AB domains as type I locations (Fig. 6a, maroon boxes), and the opposite locations as type II (Fig. 6a, orange boxes). We conducted density functional theory calculations (Supplementary Note XV), which show that the global valence band (VB) maximum at the K point is $\Delta E_{VB} = 73$ meV higher in type II locations than in type I locations (Fig. 6b). Conversely, the local conduction band (CB) minimum at the K point is $\Delta E_{CB} = 60$ meV higher in type I locations. These observations, in essence, reflect the different electronic environment of the respective layers. In addition, and consistent with previous studies, our density functional theory calculations indicate that the wavefunctions at the K point are localized in the individual layers (insets, Fig. 6b)[44].

These results give rise to two effects that split the energies of type I and type II excitons in the namesake locations. First, the two locations are expected to possess different optical bandgaps, which causes excitons in type II locations to be higher in energy by $\Delta E_0 = \Delta E_{VB} - \Delta E_{CB} = 13$ meV in the intrinsic regime (Fig. 6c).
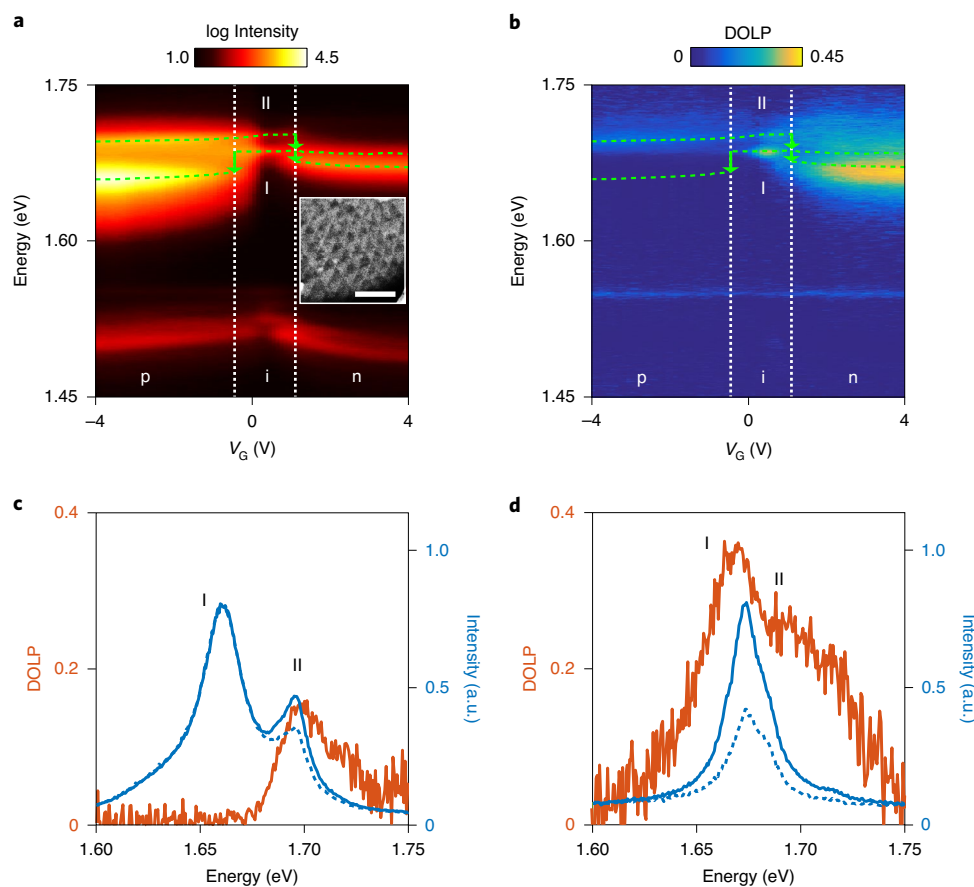
Fig. 5 | Valley coherence of the two exciton species. a, Gate-dependent PL spectra from device D1. Green dashed lines show fitted peak positions (Supplementary Note IX). Inset: SEM image of the measured spot ($\theta = 40°$). Scale bar, 200 nm. **b**, Gate-dependent DOLP, showing that type I excitons have nearly zero DOLP in the p-doped regime. **c,d**, Co- and cross-polarized PL (blue solid and dashed curves, respectively), and corresponding DOLP (orange) at $V_G = -3\,V$ (**c**) and $V_G = 2\,V$ (**d**).

This is in very good agreement with our observations for all the devices ($\Delta E_0 \approx 16\,\mathrm{meV}$; Fig. 5 and Supplementary Notes IX and X). Importantly, as $\Delta E_0 < \max(\Delta E_{VB}, \Delta E_{CB})$, our results suggest a staggered bandgap at the domain boundaries.

Second, in the doped regimes, the two exciton types are expected to have an additional energy difference because of different interactions[46] with the additional charges (Fig. 6d). In particular, our calculations predict that type I locations should be preferentially p-doped due to their higher VB maximum (Fig. 6b)[4,47]. Thus, it is indeed expected that type I excitons can bind strongly to a nearby hole to form charged excitons with a reduced energy, whereas type II excitons only interact weakly with the holes in the other layer, as found in our measurements (Figs. 3c and 5a). In the n-doped regime, our calculations indicate that the induced carriers are less layer localized than in the p-doped regime, because the global CB minimum is at the Q point instead of the K point (Fig. 6b)[48,49]. Both exciton species are therefore expected to interact with the electrons, consistent with our observations (Fig. 5a).

The higher-energy (type II) peak is only expected to be observed if the excitons are unable to relax to a lower-energy state in a different location type before recombining (exciton lifetime, $\tau_X \approx 1\text{–}10\,\mathrm{ps}$; Fig. 6e)[50,51]. Although interlayer tunnelling is symmetry forbidden at the K point in 3R (AB/BA-stacked) bilayers[4,52], moving laterally to an oppositely stacked domain within the same layer is a faster process[50,51], especially for small domains (Fig. 6e). The estimated exciton diffusion length in our system is 10–100 nm (Supplementary Note XVI), consistent with the observed disappearance of the

higher-energy peak as the domains decrease from $\lambda_m = 50\,\mathrm{nm}$ to $\lambda_m < 10\,\mathrm{nm}$. We note that for very small domains, such as in the left side of device D2 (also see the large-angle devices D8–D10 in Supplementary Note X), additional effects may appear due to the reduced effects of lattice reconstruction[9,14,21,33,34]. When the lattices are not reconstructed into perfect AB/BA domains, interlayer tunnelling is no longer symmetry forbidden (Supplementary Note XVII) and could therefore provide an additional relaxation pathway for the higher-energy state. Moreover, in the small-domain limit, the exciton wavefunction is expected to become delocalized over multiple moiré domains[9,14,40–42]. In this case, higher-energy excitons can more easily relax to lower-energy states due to their increased spatial overlap (see Supplementary Note XVII for further details).

Finally, our model also explains why the two species have such different coherence properties (Fig. 6f). In the case of type I excitons in the p-doped regime, the additional hole is in the same layer as the exciton and must therefore be in the opposite valley due to the Pauli exclusion principle (Fig. 6g). Thus, the exciton (X) and hole (h) form an entangled state $|K\rangle_X |K'\rangle_h \pm |K'\rangle_X |K\rangle_h$. As $|K\rangle_h$ and $|K'\rangle_h$ are orthogonal, linearly polarized emission is not possible[53], as observed in our experiment. For type II excitons, however, the additional holes are in the opposite layer compared with that of the exciton and thus carry no information about its valley, which allows for higher coherence than that of type I (Fig. 6h)[43,53]. In the intrinsic regime, there are no additional holes, and the DOLP of both exciton types is therefore non-zero. Finally, in the n-doped regime, the K-K exciton and resident Q-valley electron are in different valleys. Thus,
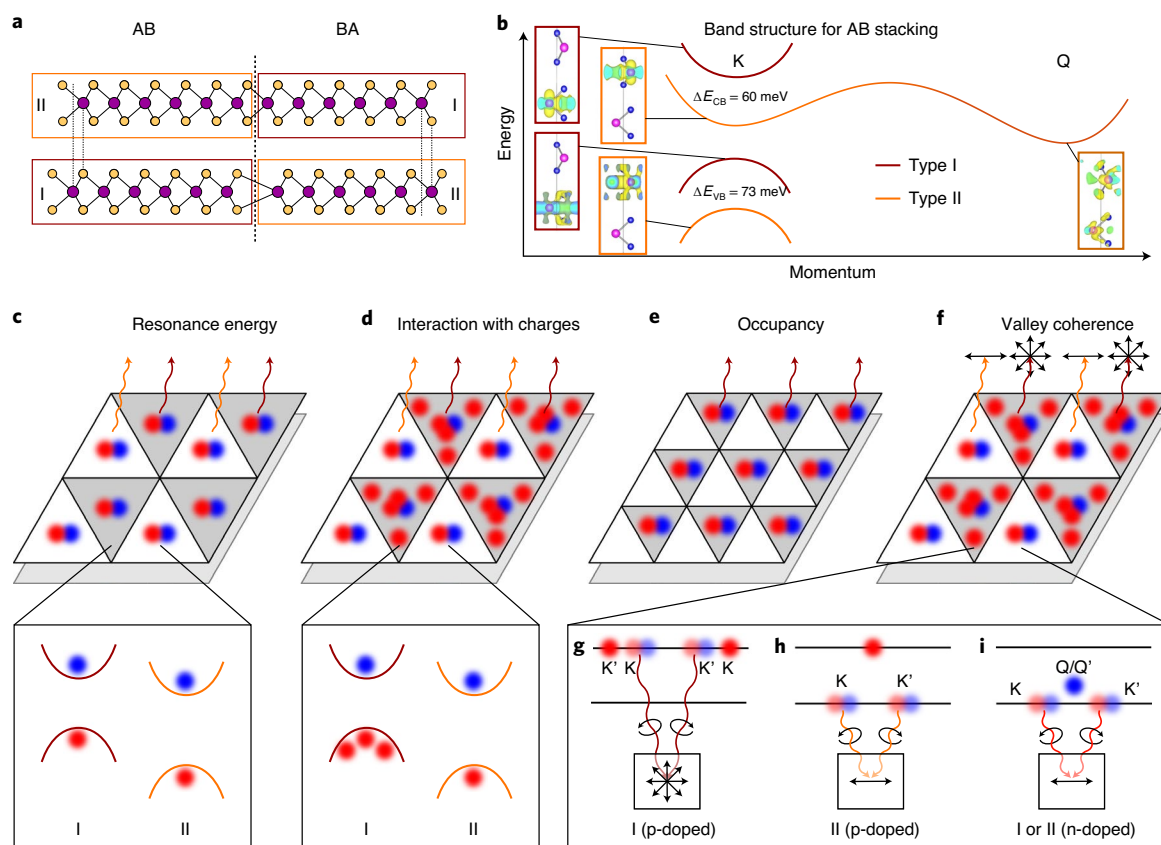
Fig. 6 | Periodic exciton and doping landscape in a reconstructed superlattice. a, Side views of AB and BA domains. Maroon and orange boxes indicate type I and II locations, respectively. **b**, Band structure schematic and wavefunction distribution at important points in *k*-space. **c–f**, Schematic of alternating properties in the 2D triangular exciton array. For clarity, only excitons in the top layer are shown. **c**, Excitons have higher energies in type II locations due to their larger optical bandgap. **d**, Type I excitons are preferentially p-doped due to a higher VB maximum. **e**, Only the type I exciton is observed in the small-domain regime due to relaxation of the higher-energy exciton. **f**, The two alternating exciton species also have different valley coherence properties. **g–i**, Schematics of K/K′ exciton recombination. The black horizontal lines indicate top and bottom layers. **g**, As the resident hole must be in the opposite valley of the type I exciton, it becomes correlated with the photon and breaks coherence. **h**, For the type II exciton, the resident hole is in a different layer and carries no information about the exciton valley, allowing for a non-zero DOLP. **i**, DOLP is non-zero for both exciton types in the n-doped regime, because the electron is in a different valley (Q/Q′) to that of the exciton (K/K′).

there is no Pauli exclusion principle at play, which allows non-zero DOLP regardless of which layer the exciton resides in (Fig. 6i).

Outlook

We have demonstrated that the SEM-based technique can be used to directly image stacking domains in bi- and few-layer graphene and, importantly, in moiré patterns in twisted vdW heterostructures. This versatile technique, which can be applied to a wide range of systems based on 2D materials (Supplementary Notes III and XVIII–XX), can also become an important tool in the pursuit of the large-area synthesis of high-quality 2D materials through techniques such as chemical vapor deposition[54]. The ability to directly resolve angle misalignment between subsequently grown layers, as well as AB, BA and AA′ stacking orders, can provide structural information on as-grown samples without a dedicated preparation for transmission electron microscopy, which thus substantially accelerates the rate of process development for material synthesis (Supplementary Note XXI).

Crucially, we have demonstrated that our technique can be used to correlate the local moiré structure with optical properties. Our observations can be understood as resulting from the emergence of two spatially alternating exciton species in the reconstructed moiré superlattice, with distinct gate tunability and valley

coherence properties. We note that, although the bilayer system as a whole is expected to exhibit the same optical response in AB and BA domains, the two layers can be treated independently due to strongly suppressed interlayer tunnelling in AB/BA domains at the K point[4]. Furthermore, a modest vertical electric field (∼0.1 V nm^{-1}) can lift the degeneracy in the AB/BA optical response in the doped regimes. Our experiments therefore indicate that this system can be an attractive solid-state platform to engineer arrays of emitters, and open the door to new quantum optoelectronic applications[3–5,7]. In particular, the large range of attainable moiré wavelengths in homobilayers, combined with electrostatic control of the individual regions, can be used to develop new types of moiré-based metasurfaces[5]. Specifically, we have shown that the splitting between type I and II excitons can be electrostatically tuned from 36 meV in the p-doped regime to 10 meV in the n-doped regime. Moreover, the tunable quantum coherence properties demonstrated in our system can enable controlled, spatially patterned entangled states of light, essential for the development of quantum metasurfaces[5].

One particularly intriguing direction involves realizing 1D localized exciton states, in which the electron and hole reside at opposite sides of the sharp moiré domain boundaries in twisted homobilayers. These have been predicted to exhibit large in-plane dipole moments, as well as quantum confinement effects in

10–100-nm-sized triangles[55]. Besides featuring triangular domains with ideal band alignment and length scales, our platform provides regular arrays of such systems, which could permit tunable interactions. This may be utilized for engineering strongly correlated states with a strong optical response, and potentially enables the realization of interacting excitons for applications such as quantum non-linear optics[5].

Online content

References

1. Mazurenko, A. et al. A cold-atom Fermi–Hubbard antiferromagnet. *Nature* **545**, 462–466 (2017).
2. Mak, K. F., Lee, C., Hone, J., Shan, J. & Heinz, T. F. Atomically thin MoS_2: a new direct-gap semiconductor. *Phys. Rev. Lett.* **105**, 136805 (2010).
3. Perczel, J. et al. Topological quantum optics in two-dimensional atomic arrays. *Phys. Rev. Lett.* **119**, 023603 (2017).
4. Wu, F., Lovorn, T., Tutuc, E., Martin, I. & MacDonald, A. H. Topological insulators in twisted transition metal dichalcogenide homobilayers. *Phys. Rev. Lett.* **122**, 086402 (2019).
5. Bekenstein, R. et al. Quantum metasurfaces with atom arrays. *Nat. Phys.* **16**, 676–681 (2020).
6. Wu, F., Lovorn, T., Tutuc, E. & MacDonald, A. H. Hubbard model physics in transition metal dichalcogenide moiré bands. *Phys. Rev. Lett.* **121**, 026402 (2018).
7. Yu, H., Liu, G.-B., Tang, J., Xu, X. & Yao, W. Moiré excitons: from programmable quantum emitter arrays to spin–orbit-coupled artificial lattices. *Sci. Adv.* **3**, e1701696 (2017).
8. Seyler, K. L. et al. Signatures of moiré-trapped valley excitons in $MoSe_2$/WSe_2 heterobilayers. *Nature* **567**, 66–70 (2019).
9. Tran, K. et al. Evidence for moiré excitons in van der Waals heterostructures. *Nature* **567**, 71–75 (2019).
10. Li, W., Lu, X., Dubey, S., Devenica, L. & Srivastava, A. Dipolar interactions between localized interlayer excitons in van der Waals heterostructures. *Nat. Mater.* **19**, 624–629 (2020).
11. Brotons-Gisbert, M. et al. Spin–layer locking of interlayer excitons trapped in moiré potentials. *Nat. Mater.* **19**, 630–636 (2020).
12. Alexeev, E. M. et al. Resonantly hybridized excitons in moiré superlattices in van der Waals heterostructures. *Nature* **567**, 81–86 (2019).
13. Zhang, N. et al. Moiré intralayer excitons in a $MoSe_2$/MoS_2 heterostructure. *Nano Lett.* **18**, 7651–7657 (2018).
14. Jin, C. et al. Observation of moiré excitons in WSe_2/WS_2 heterostructure superlattices. *Nature* **567**, 76–80 (2019).
15. Wang, L. et al. Correlated electronic phases in twisted bilayer transition metal dichalcogenides. *Nat. Mater.* **19**, 861–866 (2020).
16. Schrade, C. & Fu, L. Spin-valley density wave in moiré materials. *Phys. Rev. B* **100**, 035413 (2019).
17. Scuri, G. et al. Electrically tunable valley dynamics in twisted WSe_2/WSe_2 bilayers. *Phys. Rev. Lett.* **124**, 217403 (2020).
18. Xian, L. et al. Realization of nearly dispersionless bands with strong orbital anisotropy from destructive interference in twisted bilayer MoS_2. Preprint at https://arxiv.org/abs/2004.02964 (2020).
19. Kerelsky, A. et al. Moiré-less correlations in ABCA graphene. Preprint at https://arxiv.org/abs/1911.00007 (2019).
20. McGilly, L. J. et al. Visualization of moiré superlattices. *Nat. Nanotechnol.* **15**, 580–584 (2020).
21. Weston, A. et al. Atomic reconstruction in twisted bilayers of transition metal dichalcogenides. *Nat. Nanotechnol.* **15**, 592–597 (2020).
22. Xiong, L. et al. Photonic crystal for graphene plasmons. *Nat. Commun.* **10**, 4780 (2019).
23. Schwartz, A. J., Kumar, M., Adams, B. L. & Field, D. P. *Electron Backscatter Diffraction in Materials Science* Vol. 2 (Springer, 2009).
24. Coates, D. Kikuchi-like reflection patterns obtained with the scanning electron microscope. *Phil. Mag. A* **16**, 1179–1184 (1967).
25. Ashida, K., Kajino, T., Kutsuma, Y., Ohtani, N. & Kaneko, T. Crystallographic orientation dependence of SEM contrast revealed by SiC polytypes. *J. Vac. Sci. Technol. B* **33**, 04E104 (2015).
26. Chen, G. et al. Signatures of tunable superconductivity in a trilayer graphene moiré superlattice. *Nature* **572**, 215–219 (2019).
27. Martin, I., Blanter, Y. M. & Morpurgo, A. Topological confinement in bilayer graphene. *Phys. Rev. Lett.* **100**, 036804 (2008).
28. Ju, L. et al. Topological valley transport at bilayer graphene domain walls. *Nature* **520**, 650–655 (2015).
29. Vaezi, A., Liang, Y., Ngai, D. H., Yang, L. & Kim, E.-A. Topological edge states at a tilt boundary in gated multilayer graphene. *Phys. Rev. 3*, 021018 (2013).
30. Joy, D., Prasad, M. & Meyer, H. III Experimental secondary electron spectra under SEM conditions. *J. Microsc.* **215**, 77–85 (2004).
31. Mak, K. F., Shan, J. & Heinz, T. F. Electronic structure of few-layer graphene: experimental demonstration of strong dependence on stacking sequence. *Phys. Rev. Lett.* **104**, 176404 (2010).
32. Nguyen, T. A., Lee, J.-U., Yoon, D. & Cheong, H. Excitation energy dependent Raman signatures of ABA- and ABC-stacked few-layer graphene. *Sci. Rep.* **4**, 4630 (2014).
33. Yoo, H. et al. Atomic and electronic reconstruction at the van der Waals interface in twisted bilayer graphene. *Nat. Mater.* **18**, 448–453 (2019).
34. Carr, S. et al. Relaxation and domain formation in incommensurate two-dimensional heterostructures. *Phys. Rev. B* **98**, 224102 (2018).
35. van der Zande, A. M. et al. Tailoring the electronic structure in bilayer molybdenum disulfide via interlayer twist. *Nano Lett.* **14**, 3869–3875 (2014).
36. Scuri, G. et al. Large excitonic reflectivity of monolayer $MoSe_2$ encapsulated in hexagonal boron nitride. *Phys. Rev. Lett.* **120**, 037402 (2018).
37. Dibos, A. M. et al. Electrically tunable exciton–plasmon coupling in a WSe_2 monolayer embedded in a plasmonic crystal cavity. *Nano Lett.* **19**, 3543–3547 (2019).
38. Kunstmann, J. et al. Momentum-space indirect interlayer excitons in transition-metal dichalcogenide van der Waals heterostructures. *Nat. Phys.* **14**, 801–805 (2018).
39. Liu, K. et al. Evolution of interlayer coupling in twisted molybdenum disulfide bilayers. *Nat. Commun.* **5**, 4966 (2014).
40. Wu, F., Lovorn, T. & MacDonald, A. H. Topological exciton bands in moiré heterojunctions. *Phys. Rev. Lett.* **118**, 147401 (2017).
41. Wang, Y., Wang, Z., Yao, W., Liu, G.-B. & Yu, H. Interlayer coupling in commensurate and incommensurate bilayer structures of transition-metal dichalcogenides. *Phys. Rev. B* **95**, 115429 (2017).
42. Brem, S. et al. Hybridized intervalley moiré excitons and flat bands in twisted WSe_2 bilayers. *Nanoscale* **12**, 11088–11094 (2020).
43. Jones, A. M. et al. Spin–layer locking effects in optical orientation of exciton spin in bilayer WSe_2. *Nat. Phys.* **10**, 130–134 (2014).
44. Cappelluti, E., Roldán, R., Silva-Guillén, J. A., Ordejón, P. & Guinea, F. Tight-binding model and direct-gap/indirect-gap transition in single-layer and multilayer MoS_2. *Phys. Rev. B* **88**, 075409 (2013).
45. Hao, K. et al. Direct measurement of exciton valley coherence in monolayer WSe_2. *Nat. Phys.* **12**, 677–682 (2016).
46. Mak, K. F. et al. Tightly bound trions in monolayer MoS_2. *Nat. Mater.* **12**, 207–2011 (2012).
47. Kormányos, A., Zólyomi, V., Fal'ko, V. I. & Burkard, G. Tunable Berry curvature and valley and spin Hall effect in bilayer MoS_2. *Phys. Rev. B* **98**, 035408 (2018).
48. Liu, G.-B., Xiao, D., Yao, Y., Xu, X. & Yao, W. Electronic structures and theoretical modelling of two-dimensional group-VIB transition metal dichalcogenides. *Chem. Soc. Rev.* **44**, 2643–2663 (2015).
49. Nguyen, P. V. et al. Visualizing electrostatic gating effects in two-dimensional heterostructures. *Nature* **572**, 220–223 (2019).
50. Kulig, M. et al. Exciton diffusion and halo effects in monolayer semiconductors. *Phys. Rev. Lett.* **120**, 207401 (2018).
51. Cadiz, F. et al. Exciton diffusion in WSe_2 monolayers embedded in a van der Waals heterostructure. *Appl. Phys. Lett.* **112**, 152106 (2018).
52. Pisoni, R. et al. Absence of interlayer tunnel coupling of K-valley electrons in bilayer MoS_2. *Phys. Rev. Lett.* **123**, 117702 (2019).
53. Hao, K. et al. Trion valley coherence in monolayer semiconductors. *2D Mater.* **4**, 025105 (2017).
54. Mandyam, S. V. et al. Controlled growth of large-area bilayer tungsten diselenides with lateral p–n junctions. *ACS Nano* **13**, 10490–10498 (2019).
55. Lau, K. W., Calvin, Gong, Z., Yu, H. & Yao, W. Interface excitons at lateral heterojunctions in monolayer semiconductors. *Phys. Rev. B* **98**, 115427 (2018).

Methods

Device fabrication. Flakes of hBN, graphene and WSe_2 were first mechanically exfoliated from bulk crystals onto clean Si/SiO_2 wafers (Si substrates with 285 nm of thermally grown SiO_2). Few-layer graphene and monolayer WSe_2 were identified optically, and the thickness of the hBN flakes was determined with atomic force microscopy. Next, the heterostructures were assembled with the dry-transfer method, using the tear-and-stack technique[56] to form twisted bilayer WSe_2. Electrical contacts to both the WSe_2 and the graphite gates were defined with electron-beam lithography and deposited through thermal evaporation (10 nm Cr + 90 nm Au).

Measurements. Photoluminescence measurements were conducted in a 4 K cryostat (Montana Instruments), using a custom-built 4f confocal microscopy setup with a 0.75 numerical aperture objective and a 660 nm Thorlabs diode laser. Two galvo mirrors were used to control the excitation and collection positions on the sample, and electrostatic gating was performed with Keithley multimeters. The DOLP was measured with polarizers in the excitation and collection paths. To eliminate any polarization-dependent system response, all the DOLP measurements included excitation with (and collection of) both vertically and horizontally polarized light. The DOLP was then calculated from:

$$\text{DOLP} = \frac{r-1}{r+1}, \ r = \frac{\sqrt{I_{hh} \times I_{vv}}}{\sqrt{I_{vh} \times I_{hv}}},$$

where the subscripts indicate the polarization of the excitation and collection, respectively (h, horizontal; v, vertical).

SEM imaging of the reconstructed moiré pattern was done with a Zeiss Field Emission Scanning Electron Microscope Ultra Plus. Detailed parameters used to image the samples presented here can be found in Supplementary Note XXII.

Data availability

All data needed to evaluate the conclusions are presented in the article and the Supplementary Information.

References

56. Kim, K. et al. van der Waals heterostructures with high accuracy rotational alignment. *Nano Lett.* **16**, 1989–1995 (2016).

Author contributions

T.I.A., G.S., A.S., K.D.G., H.P. and M.D.L. conceived the project. T.I.A., G.S., A.S. and K.D.G. designed and performed the experiments, analysed the data and wrote the manuscript with extensive input from the other authors. Y.Z. and J.S. assisted with the optical measurements. T.I.A., G.S., J.S., Y.Z., L.A.J. and A.Y.J. fabricated the samples. A.S. and K.D.G. performed the SEM imaging. T.I.A., G.S., A.S., K.D.G, D.S.W. and D.B. developed the theoretical model. H.H. grew the TMD crystals. T.T. and K.W. grew the hBN crystals. P.K., H.P. and M.D.L. supervised the project.

Competing interests

Additional information